2017/07/10
Head Id: 415556
Archive Id: 415557P
Archive Date: 2017/07/10
Archive Tag: trunk

Search for $t\bar{t}$ resonances in highly boosted lepton+jets and fully hadronic final states in proton-proton collisions at $\sqrt{s} = 13\,\text{TeV}$

The CMS Collaboration

Abstract

A search for the production of heavy resonances decaying into top quark-antiquark pairs is presented. The analysis is performed in the lepton+jets and fully hadronic channels using data collected in proton-proton collisions at $\sqrt{s} = 13\,\text{TeV}$ using the CMS detector at the LHC, corresponding to an integrated luminosity of $2.6\,\text{fb}^{-1}$. The selection is optimized for massive resonances, where the top quarks have large Lorentz boosts. No evidence for resonant $t\bar{t}$ production is found in the data, and upper limits on the production cross section of heavy resonances are set. The exclusion limits for resonances with masses above 2 TeV are significantly improved compared to those of previous analyses at $\sqrt{s} = 8\,\text{TeV}$.

1 Introduction

Numerous extensions of the standard model (SM) predict the existence of new interactions with enhanced couplings to third-generation quarks, especially the top quark. The associated massive new particle contained in these theories could be observed as a $\mathrm{t\bar{t}}$ resonance in experiments at the CERN LHC. Examples of such resonances are: massive color-singlet Z-like bosons (Z') in extended gauge theories [1–3], colorons [4–7] and axigluons [8–10] in models with extended strong interaction sectors, heavier Higgs siblings in models with extended Higgs sectors [11], and Kaluza–Klein (KK) excitations of gluons [12], electroweak gauge bosons [13], and gravitons [14] in various extensions of the Randall–Sundrum (RS) model [15, 16]. These models predict the existence of TeV-scale resonances with production cross sections of a few picobarns at $\sqrt{s} = 13\,\mathrm{TeV}$. In all of these examples, resonant $\mathrm{t\bar{t}}$ production would be observable in the reconstructed invariant mass spectrum of the top quark-antiquark pair ($M_{\mathrm{t\bar{t}}}$).

Searches performed at the Tevatron have set upper limits on the production cross section of narrow Z' resonances with masses below 900 GeV that decay into $\mathrm{t\bar{t}}$ and have a relative decay width Γ/M of 1.2% [17, 18]. Similarly, searches at the LHC have set sub-picobarn limits on the production cross section of resonances in the 1–3 TeV mass range [19–26] at $\sqrt{s} = 7$ and 8 TeV. The most stringent limits are from the CMS 8 TeV analysis [27], which combines searches in the fully hadronic, lepton+jets, and dilepton+jets channels. This work excludes narrow (1.2% relative width) and wide (10% relative width) Z' bosons with masses of up to 2.4 and 2.9 TeV, respectively, and an RS KK gluon with mass of up to 2.8 TeV, at the 95% CL.

In this paper, we present a search for the production of heavy spin-1 or spin-2 resonances decaying into $\mathrm{t\bar{t}}$ pairs using the analysis methods described in Ref. [27]. We use data recorded in 2015 with the CMS detector in proton-proton (pp) collisions at $\sqrt{s} = 13\,\mathrm{TeV}$ at the LHC, corresponding to an integrated luminosity of $2.6\,\mathrm{fb}^{-1}$. Four benchmark models are considered: a Z' boson decaying exclusively to $\mathrm{t\bar{t}}$ with relative decay widths of 1%, 10%, and 30%, and a KK gluon resonance in the RS model (having a relative decay width of approximately 17%). The Z' events are generated in the framework of the sequential SM (SSM) [28]. Although the 1% and 30% widths are unphysical for various masses in that model, assuming SM-like couplings to quarks, this approach enables us to present limits as a function of width, allowing the results to be reinterpreted in models with different resonance widths. The RS KK gluon model is provided as an example of a specific, well-motivated model with a predicted physical width.

A search is performed using the $M_{\mathrm{t\bar{t}}}$ spectrum for resonances with masses greater than 500 GeV, where the top quarks from the resonance decay have large Lorentz boosts. The analysis is performed using the lepton+jets and fully hadronic $\mathrm{t\bar{t}}$ decay modes. The lepton+jets channel is

$$\mathrm{t\bar{t}} \to (\mathrm{W^+b})(\mathrm{W^-\bar{b}}) \to (\mathrm{q_1\bar{q}_2b})(\ell^-\bar{\nu}_\ell\mathrm{\bar{b}}) \qquad \text{(or charge conjugate)},$$

where one W boson decays hadronically, and the other decays to a muon or an electron, and the associated neutrino. The fully hadronic channel is

$$\mathrm{t\bar{t}} \to (\mathrm{W^+b})(\mathrm{W^-\bar{b}}) \to (\mathrm{q_1\bar{q}_2b})(\mathrm{q_3\bar{q}_4\bar{b}}),$$

where both W bosons decay hadronically. The sensitivity of the search is improved by identifying jets originating from the hadronization of b quarks (b jets), and separating the samples into categories that depend on the number of leptons (0 or 1), the lepton flavor (electron or muon), the number of jets consistent with a hadronic top quark decay ("t-tagged" jets), and the number of b jets or b subjets (where subjets are smaller jets found within a given jet). In the lepton+jets channel, the resulting samples consist mainly of events from SM $\mathrm{t\bar{t}}$ production or from W boson production in association with jets. In the fully hadronic channel, the resulting samples are

dominated by SM $\mathrm{t\bar{t}}$ and non-top multijet production. We refer to the latter as NTMJ, and this category comprises events from quantum chromodynamic (QCD) interactions as well as from other processes that result in jet production. The term "QCD multijet" is used to describe the class of interactions considered in the generation of samples of simulated events arising solely from QCD processes.

In this paper, Section 2 describes the CMS detector, while Sections 3 and 4 describe the techniques used for object reconstruction and the properties of simulated events utilized in the analysis, respectively. Section 5 describes the event selections applied in each channel of the analysis, and Section 6 outlines the methods developed to estimate the various background components using fitting procedures. Finally, Section 7 contains the results of the analysis in the form of cross section limits on new physics models, and Section 8 summarizes the work.

2 The CMS detector

The central feature of the CMS apparatus [29] is a superconducting solenoid of 6 m internal diameter, providing a magnetic field of 3.8 T. Within the solenoid volume are a silicon pixel and strip tracker, a lead tungstate crystal electromagnetic calorimeter (ECAL), and a brass and scintillator hadron calorimeter (HCAL). In the region $|\eta| < 1.74$, the HCAL cells have widths of 0.087 in pseudorapidity (η) and 0.087 radians in azimuth (ϕ). In the η–ϕ plane, and for $|\eta| < 1.48$, the HCAL cells map on to 5×5 ECAL crystals arrays to form calorimeter towers projecting radially outwards from close to the nominal interaction point. For $|\eta| > 1.74$, the coverage of the towers increases progressively to a maximum of 0.174 in $\Delta\eta$ and $\Delta\phi$. Within each tower, the energy deposits in ECAL and HCAL cells are summed to define the calorimeter tower energies, subsequently used to provide the energies and directions of hadronic jets. Electron momenta are estimated by combining the energy measurement in the ECAL with the momentum measurement in the tracker. Extensive forward calorimetry complements the coverage provided by the barrel and endcap detectors. Muons are measured in gas-ionization detectors embedded in the steel flux-return yoke outside the solenoid. A more detailed description of the CMS detector, together with a definition of the coordinate system used and the relevant kinematic variables, can be found in Ref. [29].

3 Event reconstruction

Event reconstruction is based on the CMS particle-flow (PF) algorithm [30, 31], which takes into account information from all subdetectors, including measurements from the tracking system, energy deposits in the ECAL and HCAL, and tracks reconstructed in the muon detectors. Given this information, all particles in the event are reconstructed as electrons, muons, photons, charged hadrons, or neutral hadrons.

Primary vertices are reconstructed using a deterministic annealing filtering algorithm [32]. The leading primary vertex of the event is defined as the primary vertex with the largest squared sum of transverse momenta (p_{T}) of associated charged particles. Charged particles associated with other primary vertices due to additional interactions within the same bunch crossing ("pileup") are removed from further consideration.

Muons are reconstructed using the information collected in the muon detectors and the inner tracking detectors, and are measured in the range $|\eta| < 2.4$. Tracks associated with muon candidates must be consistent with muons originating from the leading primary vertex, and are required to satisfy identification requirements. Matching muon chamber information to

tracks measured in the silicon tracker results in a p_T resolution of 1.3–2.0% in the barrel and better than 6% in the endcaps for muons with $20 < p_T < 100\,\text{GeV}$. The p_T resolution in the barrel is better than 10% for muons with p_T up to 1 TeV [33].

Electron candidates are reconstructed in the range $|\eta| < 2.5$ by combining tracking information with energy deposits in the ECAL. Candidates are identified [34] using information on the spatial distribution of the shower, the track quality, and the spatial match between the track and electromagnetic cluster, the fraction of total cluster energy in the HCAL, and the level of activity in the surrounding tracker and calorimeter regions. The transverse momentum resolution for electrons with $p_T \approx 45\,\text{GeV}$ from $Z \to ee$ decays ranges from 1.7% for nonshowering electrons in the barrel region to 4.5% for electrons showering in the endcaps [34].

Jets are clustered using PF candidates as inputs to the anti-k_T algorithm [35] in the FastJet 3.0 software package [36] using two different choices of the distance parameter: $R = 0.4$ and 0.8. In the following, we refer to the first set of jets as AK4 or small-radius jets, and the second set of jets as AK8 or large-radius jets. For both the small- and large-radius jets, corrections based on the jet area [37] are applied to the energy of the jets to remove the energy contributions from neutral hadrons from pileup interactions. Subsequent corrections are used to account for the combined response function of the calorimeters in both jet energy and mass, as a function of η and p_T [38]. The jet energy resolution varies from 15% at 10 GeV to 8% at 100 GeV to 4% at 1 TeV for the small-radius jets, and degrades by a few percent for the large-radius jets. The small-radius jets associated with b quarks are identified using the Combined Secondary Vertex v2 (CSVv2) algorithm [39, 40]. The working point used for jet b tagging in this analysis has an efficiency of ≈65% (in $t\bar{t}$ simulated events) and a mistag rate (the fraction of light-flavor jets that are incorrectly tagged) of ≈1% [40].

The large-radius jets with $p_T > 500\,\text{GeV}$ are taken as hadronic top quark candidates. To identify true top quark decays, the "CMS top tagger v2" algorithm [41] is used. In this algorithm, the constituents of the AK8 jets are reclustered using the Cambridge–Aachen algorithm [42, 43]. The "modified mass drop tagger" algorithm [44], also known as the "soft drop" (SD) algorithm, recursively declusters a jet into two subjets, discarding soft and wide-angle radiation jet components until a hard splitting criterion is met, to obtain jets consistent with boosted heavy-object decays. This algorithm has been shown to improve jet mass resolution by approximately 40% relative to standard reconstruction techniques [45]. The algorithm is used with angular exponent $\beta = 0$, soft cutoff threshold $z_{cut} < 0.1$, and characteristic radius $R_0 = 0.8$ [46]. This algorithm is also able to identify two subjets within the AK8 jet. The subjet corresponding to the b quark can be identified using subjet b tagging techniques [39]. Specifically, the CSVv2 algorithm, as described above, identifies b-tagged subjets. The algorithm has a comparable performance when applied to subjets, but the uncertainties are larger because of the limited number of highly boosted objects used to measure its efficiency. The N-subjettiness observables τ_N are calculated using all PF candidates in the AK8 jet. Each corresponds to a p_T-weighted minimum distance from one of N hypothesized subjet axes, defined by the one-pass minimization procedure. These observables are used to quantify the consistency of the particles of a jet with an N-prong decay topology. The variable $\tau_{32} = \tau_3/\tau_2$ [47, 48] is employed to identify the three-pronged substructure of a hadronically decaying top quark. The specific working point used in this analysis is defined by requiring that the soft-dropped mass of the jet satisfies $110 < M_{SD} < 210\,\text{GeV}$ and the N-subjettiness variable satisfies $\tau_{32} < 0.69$, which corresponds to a misidentification rate (for light-flavor quark and gluon jets) in simulation of 3% [41]. This working point selects top quark jets with an efficiency of approximately 40% when the jet p_T is above 500 GeV. Jets selected by the jet mass and N-subjettiness criteria are referred to as "t-tagged". Additionally, t-tagged jets are considered to have a subjet b tag if

they contain at least one soft-dropped subjet identified as b-tagged using the working point described above.

The missing p_T in the plane transverse to the beam direction is reconstructed as the negative vector sum of the p_T of all PF candidates reconstructed in the event [38]. Its magnitude is denoted by p_T^{miss}. Corrections to the jet energy scale and jet energy resolution are propagated to the measurement of p_T^{miss}.

4 Simulated events

The simulation of Z′ resonances is performed with the leading-order MADGRAPH v5.2.2.2 [49] Monte Carlo (MC) program using SM values for the left- and right-handed Z′ couplings to top quarks. The simulation is performed for a range of Z′ masses between 0.5 and 4.0 TeV, and for the three relative width hypotheses of 1%, 10%, and 30%. Higher-order QCD multijet processes for up to three extra partons are simulated at tree level. The Z′ boson is required to decay into a $t\bar{t}$ pair in all generated events. The parton showering and hadronization is modeled with PYTHIA 8.205 [50, 51], and the MLM algorithm [52] is used to match the parton shower to the matrix element calculation with a merging scale of 35 GeV.

The simulation of KK excitations of a gluon is performed with the PYTHIA program. The KK gluon excitations are simulated with resonance masses between 0.5 and 4.0 TeV, assuming the branching fraction of the KK gluon into top quark pairs is ≈ 94%, with the branching fraction to bottom (light) quark pairs being 5% (<1%) [12]. Figure 1 shows the generator-level $M_{t\bar{t}}$ distributions for resonance masses of 2 TeV and 4 TeV, for the various signal hypotheses considered. For the highest-mass samples considered, the resonance production is dominated by off-shell contributions, giving the long tail toward low values of $M_{t\bar{t}}$ seen in the distributions.

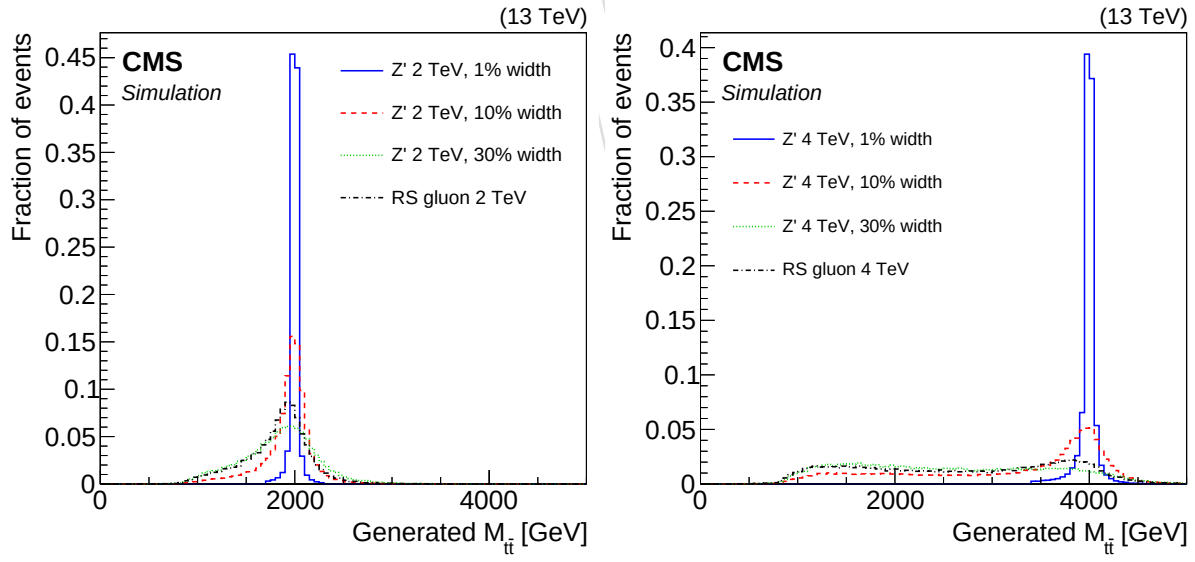

Figure 1: Distributions of generator-level $M_{t\bar{t}}$ for the production of new particles with masses of 2 TeV (left) and 4 TeV (right), for the four signal hypotheses considered in this analysis.

Background events from $t\bar{t}$ production via QCD interactions and electroweak production of single top quarks in the tW channel are simulated with the next-to-leading order (NLO) generator POWHEG (v2) [53–57]. The *s*- and *t*-channel processes of single top quark production are simulated with MADGRAPH5_aMC@NLO v5.2.2.2 [49]. All events are interfaced with PYTHIA for the description of fragmentation and hadronization.

The associated production of W or Z boson and jets is simulated using MADGRAPH. The MLM matching scheme is applied to match the showers generated with PYTHIA. Up to four additional partons in the matrix element calculations are included. The $t\bar{t}$, W/Z+jets, and single-top-quark samples are normalized to the theoretical predictions described in Refs. [58–61]. Diboson processes (VV = WW, WZ, and ZZ) are simulated with PYTHIA for both the matrix element and parton showering calculations. The event rates are normalized to the NLO cross sections from Ref. [62].

Simulated QCD multijet events, generated with PYTHIA, are used to validate the background-estimation procedure in the fully hadronic channel, but not in the search, where the NTMJ background is estimated from sideband regions in data.

All events are generated at the center of mass energy of 13 TeV and use the NNPDF 3.0 parton distribution functions (PDF) [63]. In the parton shower simulated with PYTHIA, the underlying event tune CUETP8M1 [64, 65] has been used. All simulated samples include the effects of additional inelastic proton-proton interactions within the same or adjacent bunch crossings.

5 Event selection and categorization

5.1 Lepton+jets channel

Events in the muon channel are collected with a single-muon trigger, which requires the presence of a muon with $p_T > 45\,\text{GeV}$ and $|\eta| < 2.1$. The trigger selection employed in the electron channel requires an electron with $p_T > 45\,\text{GeV}$, $|\eta| < 2.5$, and at least two jets with $p_T > 200$ (50) GeV for the leading (subleading) AK4 jet reconstructed at trigger level. These trigger choices ensure an efficiency of about 99% for high-mass signal events.

In the lepton+jets analysis, we select events offline containing one muon with $p_T > 50\,\text{GeV}$ and $|\eta| < 2.1$ or one electron with $p_T > 50\,\text{GeV}$ and $|\eta| < 2.5$, and at least two AK4 jets with $|\eta| < 2.4$. In the muon (electron) channel, the leading AK4 jet is required to have $p_T > 150$ (250) GeV, and the subleading AK4 jet must have $p_T > 50$ (70) GeV. Additional reconstructed jets, utilized in the reconstruction of the $t\bar{t}$ system, are required to have $p_T > 30\,\text{GeV}$. Given the highly-boosted topology of the final-state objects, no isolation requirements are applied to the leptons at the trigger level or in the analysis stages. However, events are required to pass a two-dimensional selection of $\Delta R(\ell, j) > 0.4$ or $p_T^{\text{rel}}(\ell, j) > 20\,\text{GeV}$, where j is the small-radius jet with minimal angular separation $\Delta R = \sqrt{(\Delta\eta)^2 + (\Delta\phi)^2}$ from the lepton ℓ (electron or muon), and $p_T^{\text{rel}}(\ell, j)$ is the component of the lepton momentum orthogonal to the axis of jet j. The values of $\Delta R(\ell, j)$ and $p_T^{\text{rel}}(\ell, j)$ are calculated considering small-radius jets with $p_T > 15\,\text{GeV}$ and $|\eta| < 3.0$. The values used are optimized for this analysis. This two-dimensional selection effectively replaces the more conventional lepton isolation requirement, as it significantly reduces the background from NTMJ production while maintaining high efficiency for the high-mass signal hypotheses.

Events in the muon channel are required to have $p_T^{\text{miss}} > 50\,\text{GeV}$ and $(p_T^{\text{miss}} + p_T^{\ell}) > 150\,\text{GeV}$. In the electron channel, where jets are often misidentified as electrons, we find that the most effective approach for rejecting NTMJ events is to require only $p_T^{\text{miss}} > 120\,\text{GeV}$. After these requirements, the contributions from NTMJ production in both lepton channels are found to be negligible. We also reject events that contain a second lepton to ensure there is no overlap between the event samples and to maintain a clear distinction between lepton+jets and dilepton+jets analyses. Finally, we veto events with two t-tagged jets to ensure orthogonality to the fully hadronic analysis. This veto has a negligible impact on the signal efficiency of the

lepton+jets analysis.

The kinematic reconstruction of the $t\bar{t}$ system in the lepton+jets channel is performed by assigning the products in the final state to either the leptonic or hadronic branch of the $t\bar{t}$ system. We first assign the charged lepton and p_T^{miss} to the leptonic branch of the event, where p_T^{miss} is interpreted as the p_T of the neutrino, $p_z(\nu)$. The longitudinal component of the neutrino momentum is inferred by constraining the invariant mass of the $\ell + \nu$ system to match the W boson mass. This procedure leads to a quadratic equation in $p_z(\nu)$. If two real solutions are found, hypotheses are built for both cases. If no real solutions are available, the real part is taken as $p_z(\nu)$. In events without t-tagged jets, only small-radius jets are used to reconstruct both the leptonic and hadronic top decays.

In events containing a t-tagged jet, the large-radius jet is assigned to the hadronically decaying top quark. Only small-radius jets with a separation of $\Delta R > 1.2$ from the t-tagged jet are used in the reconstruction of the leptonic top quark decay. Because of the presence of multiple $t\bar{t}$ hypotheses per event, a two-term χ^2 discriminator is used to quantify the compatibility of each hypothesis with a $t\bar{t}$ decay. The discriminator is defined as

$$\chi^2 = \left(\frac{M_{lep} - \overline{M}_{lep}}{\sigma_{M_{lep}}} \right)^2 + \left(\frac{M_{had} - \overline{M}_{had}}{\sigma_{M_{had}}} \right)^2, \quad (1)$$

where M_{lep} and M_{had} are the invariant masses of the reconstructed semileptonically and hadronically decaying top quark, respectively. The quantities $\sigma_{M_{lep}}$ and $\sigma_{M_{had}}$ are the resolutions of the leptonic and hadronic top quark reconstruction, respectively, and $\overline{M}_{lep}$ and $\overline{M}_{had}$ are the means of the corresponding mass distributions. The values of $\overline{M}_{lep}$, $\sigma_{M_{lep}}$, $\overline{M}_{had}$, and $\sigma_{M_{had}}$ are derived using a sample of simulated events in which all four partons of the final state top quark decay products are matched to a reconstructed jet used in the hypothesis. In each event, the $t\bar{t}$ pair reconstructed with the smallest value of χ^2 (labeled χ^2_{min}) is chosen. In events with a t-tagged jet, M_{had} is given by the mass of the large-radius jet calculated using the soft drop algorithm. This choice is made because, compared to the conventional jet mass, the soft dropped mass is much less dependent on the jet p_T, and therefore on the resonance mass in a given signal hypothesis. Moreover, this provides greater discrimination between background and signal.

Events in the signal region are required to have $\chi^2_{min} < 30$ for all lepton+jets categories. This upper threshold on χ^2_{min} reduces the contribution of events from non-$t\bar{t}$ background processes and maximizes the expected sensitivity of the analysis to new resonances.

Finally, to further enhance sensitivity, events are categorized according to the number of t-tagged and b-tagged jets as follows : events with one t-tagged jet (1 t tag); events with zero t-tagged jets and at least one b-tagged jet (0 t tag, 1 b tag); and events with zero t-tagged and b-tagged jets (0 t tag, 0 b tag).

5.2 Fully hadronic channel

The fully hadronic channel requires that at least two jets satisfy kinematic and t tagging selection criteria. The data were collected online with a trigger requiring the scalar sum of the AK4 jet energies (H_T) to be larger than 800 GeV. The trigger selection has an efficiency of above 95%, as measured in simulation, for events that satisfy the offline requirement $H_T > 1000$ GeV. The event reconstruction is performed using only AK8 jets. The two leading jets are required to have $p_T > 500$ GeV, rapidity $|y| < 2.4$, and both are required to be t tagged. A back-to-back topology is selected by requiring the azimuthal separation of the two leading jets to satisfy $|\Delta\phi| > 2.1$.

Events are further categorized into six regions based on two criteria: the rapidity difference (Δy) between the two AK8 jets and the number of jets with at least one b-tagged subjet for the two highest p_T jets. Events can contain 0, 1, or 2 jets with a b-tagged subjet, and they are separated into bins of $|\Delta y| < 1.0$ and $|\Delta y| > 1.0$.

5.3 Tagging variables in lepton+jets and fully hadronic channels

The distributions of the two variables used in the t tagging algorithm, τ_{32} and M_{SD}, are shown in Fig. 2 for the lepton+jets channel (upper row) and the fully hadronic channel (lower row). Each of the figures is obtained after removing the selection on the quantity being plotted, while maintaining all other analysis-level selections. We observe good agreement between data and simulation in the lepton+jets decay channel, where simulated events are divided into contributions from generator-level top quarks and other jets from $t\bar{t}$ events and subdominant background processes. The fully hadronic channel also shows good agreement between the simulated distribution and data. The small discrepancies do not affect the analysis, as it relies on data to estimate the NTMJ contribution to the background. Some discrepancy is visible at high values of τ_{32}, however this region is excluded by the selection used for t tagging.

6 Background model and normalization

In this section, we describe the sources of the SM background and methods of background estimation for both the lepton+jets and fully hadronic channels. We then introduce the sources of systematic uncertainty considered in this analysis. Finally, we describe the treatment of the backgrounds and uncertainties in the maximum likelihood fit that is used to determine the total yield of SM processes and in the statistical analysis of data.

6.1 Lepton+jets channel

Several SM processes contribute to the sample obtained from the lepton+jets selection described in Section 5. The two main background processes are $t\bar{t}$ and W+jets production. The latter accounts for a sizeable portion of the background in the (0 t tag, 0 b tag) category, whereas the former fully dominates the (0 t tag, 1 b tag) and (1 t tag) categories. Single top quark, Z+jets, and diboson production contribute only a small fraction of the background.

The distributions obtained from simulation are corrected to account for known discrepancies in the observed number of data and simulated events. In particular, we derive a scale factor (SF) between data and simulation for the t tagging mistag (t mistag) rate for AK8 jets from a sample dominated by W+jets, selected by requiring events to have $\chi^2_{min} > 30$. The remaining contamination from $t\bar{t}$ is removed by subtracting the distribution of $t\bar{t}$ events in simulation. The t mistag rate is measured separately for the muon and electron channels, in data and simulation. The resulting values, together with the data-to-simulation SFs, are shown in Table 1. As the SFs for the muon and electron channels are consistent, the weighted average is used: $SF_\ell = 0.79 \pm 0.15$.

Table 1: The mistag rates in data and simulation, and their ratio (data/simulation SF), for AK8 jets in the lepton+jets analysis.

Channel	Eff. in data	Eff. in MC	SF
e+jets	0.038 ± 0.010	0.051 ± 0.002	0.74 ± 0.20
μ+jets	0.043 ± 0.012	0.051 ± 0.002	0.85 ± 0.24

The final background estimates in this search are determined by fitting the background-only

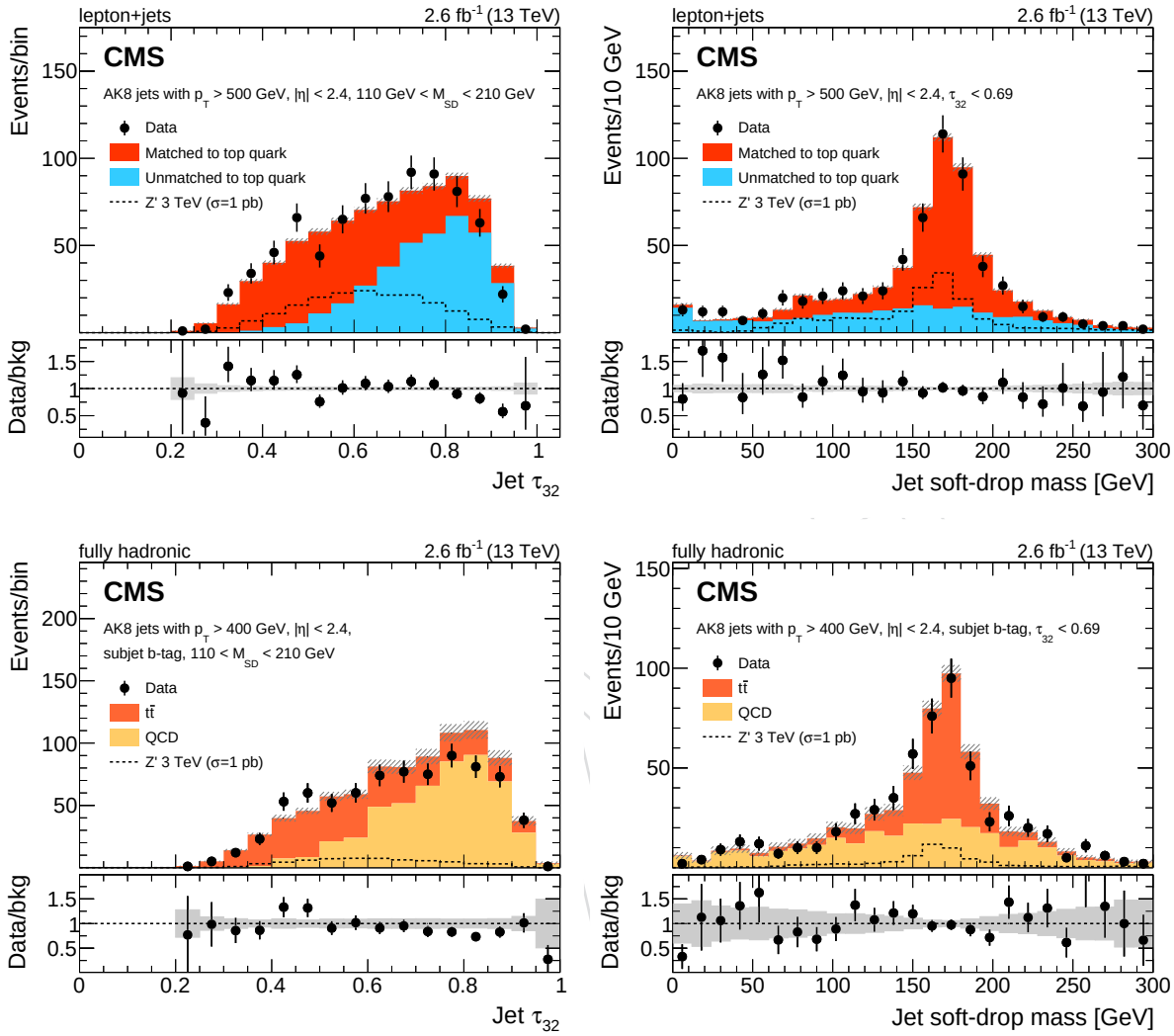

Figure 2: Distributions of the N-subjettiness ratio, τ_{32}, and the soft dropped mass, M_{SD}, for AK8 jets in data and simulation, after the signal selection. For lepton+jets, with $p_{\mathrm{T}} > 500\,\mathrm{GeV}$ (upper row). For the fully hadronic final state, with $p_{\mathrm{T}} > 400\,\mathrm{GeV}$ and subjet b tag (lower row). The distribution of τ_{32} (left) is shown after the selection $110 < M_{\mathrm{SD}} < 210\,\mathrm{GeV}$, and the distribution of M_{SD} (right) is shown after the selection $\tau_{32} < 0.69$. The lepton+jets channel plots compare data to background simulation, where the latter is divided into contributions from jets matched at the generator level to top quarks and other jets in top pair or W+jets events. The fully hadronic channel plots compare data to $\mathrm{t\bar{t}}$ and QCD multijet simulation. Contributions from a benchmark narrow Z′ signal model are shown with the black dashed lines. In obtaining the final results, NTMJ production is estimated from data, and simulated QCD multijet events are not used. In all plots, the error bars include only statistical contributions.

hypothesis to data [66]. Distributions defined in samples dominated by various backgrounds are used simultaneously in a binned maximum likelihood fit to constrain the different uncertainties in the background model using the data. The reconstructed $M_{t\bar{t}}$ distribution is used in regions dominated by $t\bar{t}$ and W+jets, and the dimuon invariant mass is used in a region dominated by Z+jets. The $t\bar{t}$-dominated region is defined by $M_{t\bar{t}} < 2\,\text{TeV}$ and $\chi^2_{\text{min}} < 30$. The region dominated by W+jets events is defined by $\chi^2_{\text{min}} > 30$. For each of these two latter regions, six exclusive categories are defined based on lepton flavor and number of b-tagged and t-tagged jets ((1 t tag); (0 t tag, 1 b tag); (0 t tag, 0 b tag)), giving a total of 12 control regions (CRs). One additional CR, dominated by Z+jets, is defined by removing the lepton veto from the μ+jets selection and adding the Z boson mass window requirement $71 < M_{\mu\mu} < 111\,\text{GeV}$. The $Z \to ee$ channel is not used because of the stringent requirement on $p_{\text{T}}^{\text{miss}}$.

6.2 Fully hadronic channel

The fully hadronic channel has two primary sources of SM background: $t\bar{t}$ events and NTMJ production. The shape of the $M_{t\bar{t}}$ distribution for $t\bar{t}$ events is taken from simulation. The normalization of this distribution is initially set to the theoretical cross section, but is allowed to vary within both rate and shape uncertainties during the statistical analysis. The shape and normalization are both fitted and extracted for each of the six event categories. The variation of the $t\bar{t}$ contribution to the total background predominantly affects the signal regions with two subjet b tags, which have $t\bar{t}$ as the dominant background component.

For the NTMJ estimate, we use a data-driven technique similar to that described in Ref. [25]. The method involves selecting a sample of data events with low SM $t\bar{t}$ contribution by inverting the t tagging N-subjettiness requirement on one selected jet (anti-tag), and determining the t tagging rate for the second jet (probe). The anti-tag jet is required to satisfy $110 < M_{\text{SD}} < 210\,\text{GeV}$ and $\tau_{32} > 0.69$. This "anti-tag and probe" method yields a per-jet t mistag rate parameterized as a function of jet momentum (which is more closely tied to the radiation within the jet than is the p_{T}) and is measured separately for events falling into each of the six b tag and $|\Delta y|$ categories (Fig. 3). The anti-tag requirement is designed to select a sample in data dominated by NTMJ events. A small number of genuine $t\bar{t}$ events survive this selection. This contamination is removed by subtracting the distributions measured in $t\bar{t}$ simulation from those measured in the anti-tag and probe selection in data.

Once the t mistag rate has been determined from the NTMJ control sample, it is used to estimate the normalization and shape of NTMJ events passing the final event selection. To do this, we use a "single-tagged" region that contains events with at least one t-tagged jet. To avoid bias, we randomly select one of the two leading top quark jet candidates and require that it pass the t tagging selection described above. If the randomly chosen jet is t tagged, we include this event and weight it by the appropriate t mistag rate based on the momentum of the jet opposite the tagged jet, their rapidity difference, and the number of subjet b tags, as shown in Fig. 3.

This singly-tagged control region without any requirements on the second jet has an overlap with the signal region, and is used to estimate the NTMJ background. To remove the effects of double-counting, the $t\bar{t}$ contribution is subtracted from the NTMJ estimate. This is done by evaluating the t mistag weighting procedure described above on the simulated $t\bar{t}$ events, to find the contribution of $t\bar{t}$ events that would enter the NTMJ background estimate when the method is applied to data. This contribution amounts to a $t\bar{t}$ contamination of about 1–2% of the NTMJ background estimate in the 0 b-tag event regions (about 6–10% in the other regions), and is subtracted from the NTMJ background estimate.

As a final step in determining the shape of the NTMJ background estimate, we correct for

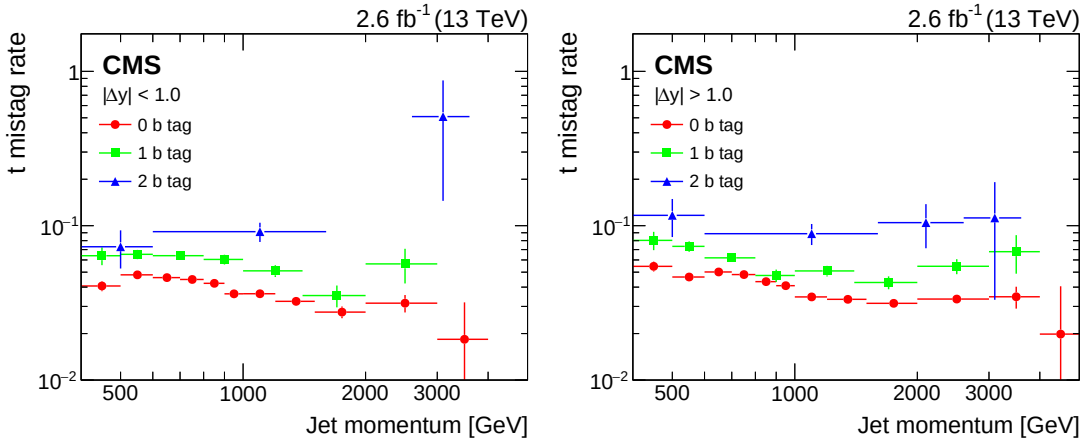

Figure 3: The mistag rate for the t tagging algorithm in the fully hadronic channel, measured with data for the six event categories by an anti-tag and probe procedure. The round, square, and triangular points indicate the t mistag rate for events in the 0, 1, and 2 b tag categories, respectively. The left (right) plot contains events with $|\Delta y| < 1.0$ (> 1.0). The contamination from $t\bar{t}$ production is removed by subtracting the distribution of $t\bar{t}$ events in simulation, normalized to SM expectation.

the fact that the second jet, having no t tagging applied, has different kinematics than jets in the signal region. To mimic the kinematics of the signal region, a "mass-modified" procedure is used, in which we randomly set the mass of this second jet according to a distribution of jet masses from simulated QCD multijet events, using the same window as used to select the signal region selection, $110 < M_{SD} < 210$ GeV. This method is validated using simulated QCD multijet events.

6.3 Systematic uncertainties

Several sources of systematic uncertainties are considered in this search. Each of these is related to an experimental uncertainty introduced in the reconstruction of the event or to a theoretical uncertainty affecting the simulation of certain background or signal processes. In particular, we quantify the effect of each of these uncertainties on the measurement of the invariant mass of the reconstructed $t\bar{t}$ system. These uncertainties are taken into account in the maximum likelihood fit to determine the total yield of SM processes, and in the statistical interpretation of the data. The complete list of systematic uncertainties is given below, and Table 2 lists the sources of uncertainty and the channels they affect.

The effect of the uncertainties in the theoretical SM cross sections for $t\bar{t}$, W+jets and Z+jets production are obtained from the background fit described above, and are 8% for $t\bar{t}$, 6% for W+jets, and 20% for Z+jets production. Small contributions to the event yields arise from single top quark and diboson production. Their normalization is taken from theory [60, 67–70] and assigned a 20% uncertainty. The effect due to missing higher-order corrections in the simulation of $t\bar{t}$ and W+jets production in the SM is estimated by varying the renormalization and factorization scales used in the simulation up and down independently by a factor of 2. Additionally, we account for uncertainties in the simulation of initial- and final-state radiation on the reconstruction of the $t\bar{t}$ system by using $t\bar{t}$ events simulated with different Q^2 scales used for the parton shower generation and evolution. Simulated samples for both background and signal processes are generated using PDFs from the NNPDF 3.0 set [63]. The corresponding systematic uncertainty is determined according to the procedure described in Ref. [71]. The uncertainty in the total integrated luminosity at $\sqrt{s} = 13$ TeV is 2.7% [72]. The systematic

uncertainty associated with the yield of simulated pileup events is evaluated by varying the inelastic pp cross section [73] by $\pm 5\%$ ($\sigma_{\text{inel}} = 72.0 \pm 3.6$ mb).

The systematic uncertainties related to the muon identification and trigger efficiencies are treated as uncorrelated, and both are applied as functions of the muon p_{T} and η [33]. The uncertainties are obtained by varying each corresponding data-to-simulation SF by one standard deviation. Additional systematic uncertainties of 1% and 0.5% are attributed to the identification and trigger efficiency SF measurements, respectively. Similarly, the uncertainty in the electron identification efficiency is applied as a function of the electron p_{T} and η [34]. An uncertainty of 2% is assigned to the efficiency of the electron trigger selection, and is determined from a complementary measurement of the e+jets trigger efficiency in a dilepton (eμ) control region.

The uncertainties in the data-to-simulation corrections for jet energy scale and jet energy resolution are evaluated by varying these corrections within their uncertainties, as functions of the jet p_{T} and η. Both systematic variations are also propagated to the measurement of $p_{\text{T}}^{\text{miss}}$ and the jet mass. A SF is applied to account for differing efficiencies and misidentification rates of the b tagging selection between data and simulation. Uncertainties in the SFs are measured as functions of the jet p_{T} and treated as uncorrelated. The data-to-simulation correction for the subjet b tagging algorithm efficiency is also included as an independent uncertainty and is evaluated by varying the correction within its uncertainties, as a function of jet p_{T} and η. The data-to-simulation correction for the efficiency of the t tagging selection for AK8 jets is measured in situ in the statistical analysis. This is done by leaving this parameter unconstrained in the fit. The t mistag efficiency in the lepton+jets channel (dominated by quarks from W+jets) is measured directly in a control region dominated by W+jets production with an uncertainty of 19%. The t mistag rate in the fully hadronic channel (dominated by gluons from QCD interactions) is measured as described above, with a momentum-dependent uncertainty ranging from 5 to 100%. These uncertainties are estimated by varying the anti-tag criterion for the construction of the anti-tag and probe sample. Systematic uncertainties due to the t tagging efficiency and t mistag rate are treated as uncorrelated.

The systematic uncertainty associated with the "mass-modified" procedure, which is used to correct the kinematic bias in the background estimation, is computed by taking half the difference between the uncorrected and "mass-modified" background estimates. This affects the shape and normalization of the $M_{\text{t}\bar{\text{t}}}$ distribution. Simulated QCD multijet events are used in a closure test to verify that the background estimation procedure accurately predicts the double t-tagged $M_{\text{t}\bar{\text{t}}}$ distribution. An additional systematic uncertainty is assigned to the NTMJ background estimate based on small disagreements (up to 10%) observed in the closure test, in the shape of the kinematic threshold at low values of $M_{\text{t}\bar{\text{t}}}$.

6.4 Fitting procedure

To improve the flexibility of the background model, we estimate the central values and uncertainties in several parameters through a maximum likelihood fit to data using the top quark pair invariant mass distribution, as follows. The normalizations for the background estimates using simulated events are left unconstrained in the fit. The data-to-simulation SF for the t tagging efficiency is also unconstrained and extracted from the fit. The SF for the subjet b tagging efficiency as well as the yield of events from the NTMJ background estimation method, having both p_{T} and η dependence, are allowed to vary within uncertainties, with their final values estimated by the fit. The NTMJ background is constrained using the procedure outlined in Section 6.2. All other systematic uncertainties are included as nuisance parameters in the fit, and are allowed to vary within their corresponding rate and shape uncertainties, as described

Table 2: Sources of uncertainty and the channels they affect. Uncorrelated uncertainties applied to a given channel are labeled with a $\odot$. Uncertainties that are correlated between channels are labeled with a $\oplus$. In this table, σ denotes the uncertainty in the given prior value in the likelihood fit.

Uncertainty		Channel	
Source	Prior uncertainty	Lepton+jets	Fully hadronic
$t\bar{t}$ cross section	$\pm 8\%$	$\oplus$	$\oplus$
W+jets cross section	$\pm 6\%$	$\odot$	
Z+jets cross section	$\pm 20\%$	$\odot$	
Single-top cross section	$\pm 20\%$	$\odot$	
Diboson cross section	$\pm 20\%$	$\odot$	
Integrated luminosity	$\pm 2.7\%$	$\oplus$	$\oplus$
Pileup modeling	$\pm 1\sigma$	$\oplus$	$\oplus$
Muon identification	$\pm 1\sigma(p_T, \eta)$	$\odot$	
Muon trigger	$\pm 1\sigma(p_T, \eta)$	$\odot$	
Electron identification	$\pm 1\sigma(p_T, \eta)$	$\odot$	
Electron trigger	$\pm 2\%$	$\odot$	
Jet energy scale	$\pm 1\sigma(p_T, \eta)$	$\oplus$	$\oplus$
Jet energy resolution	$\pm 1\sigma(\eta)$	$\oplus$	$\oplus$
Jet b tagging efficiency	$\pm 1\sigma(p_T, \eta)$	$\odot$	
Jet b mistag rate	$\pm 1\sigma(p_T, \eta)$	$\odot$	
Subjet b tagging efficiency	$\pm 1\sigma(p_T, \eta)$		$\odot$
Jet t tagging efficiency	unconstrained	$\oplus$	$\oplus$
Lepton+jets channel t mistag rate	$\pm 19\%$	$\odot$	
Fully hadronic channel t mistag rate	$\pm 1\sigma(p)$		$\odot$
PDFs	$\pm 1\sigma$	$\oplus$	$\oplus$
$t\bar{t}$ matrix element scale	$\pm 1\sigma$	$\oplus$	$\oplus$
$t\bar{t}$ parton shower scale	$\pm 1\sigma$	$\oplus$	$\oplus$
W+jets matrix element scale	$\pm 1\sigma$	$\odot$	
NTMJ background kinematics	$\pm 1\sigma$		$\odot$
NTMJ background closure test	$\pm 1\sigma$		$\odot$

above, using log-normal prior distributions. The best fit values obtained from this maximum likelihood evaluation are used to correct the distributions of background and signal processes.

A Bayesian statistical method [66, 74] is used to extract the upper limits at 95% confidence level (CL) on the product of the cross section and branching fraction, i.e. $\sigma(pp \to X)\,\mathcal{B}(X \to t\bar{t})$, for heavy resonances decaying to a $t\bar{t}$ pair. In order to maximize the expected sensitivity of the search, twelve exclusive categories are employed simultaneously in the statistical analysis, as described above. For each category, the observable used in the limit-setting procedure is $M_{t\bar{t}}$. A template-based shape analysis is performed using the Theta software package [66] for these $M_{t\bar{t}}$ distributions. The systematic uncertainties listed in Table 2 are introduced as individual nuisance parameters in the limit calculation. For the signal cross section parameter, we use a uniform prior distribution. The uncertainty in the data-to-simulation correction for t tagging efficiency is left unconstrained, whereas each of the other nuisance parameters corresponding to a systematic uncertainty is modeled with a log normal prior distribution. The uncertainty due to the finite size of the simulated samples is introduced in the statistical analysis according to the "Barlow–Beeston lite" method [75]. The impact of the statistical uncertainty in the simulated samples is limited by rebinning each $M_{t\bar{t}}$ distribution to ensure that the statistical uncertainty associated with the expected background is less than 30% in each bin.

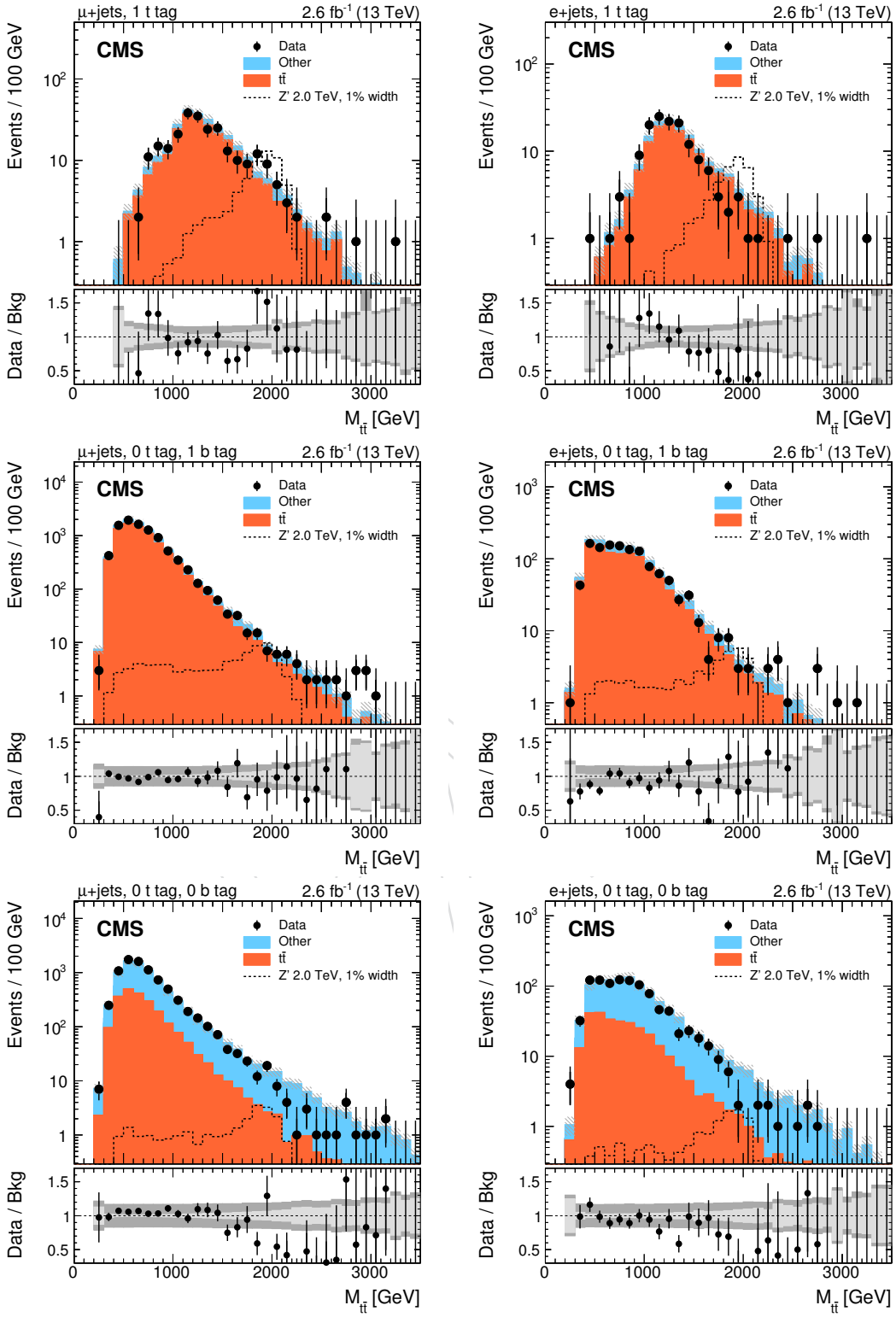

Figure 4: Distributions in $M_{\mathrm{t\bar{t}}}$ for data and expected background, for events passing the signal selection of the lepton+jets analysis ($\chi^2 < 30$) after the maximum likelihood fit. Distributions are shown for the muon (left) and electron (right) channel. For each lepton flavor, events are split into three exclusive categories (from uppermost to lowest): $(1\,\mathrm{t\ tag})$, $(0\,\mathrm{t\ tag}, 1\,\mathrm{b\ tag})$, and $(0\,\mathrm{t\ tag}, 0\,\mathrm{b\ tag})$. The signal templates are normalized to a cross section of 1 pb. The uncertainties associated with the background expectation include the statistical and all post-fit systematic uncertainties. The lower panel in each figure shows the ratio of data to predicted SM background, with the statistical (light gray) and total (dark gray) uncertainties shown separately.

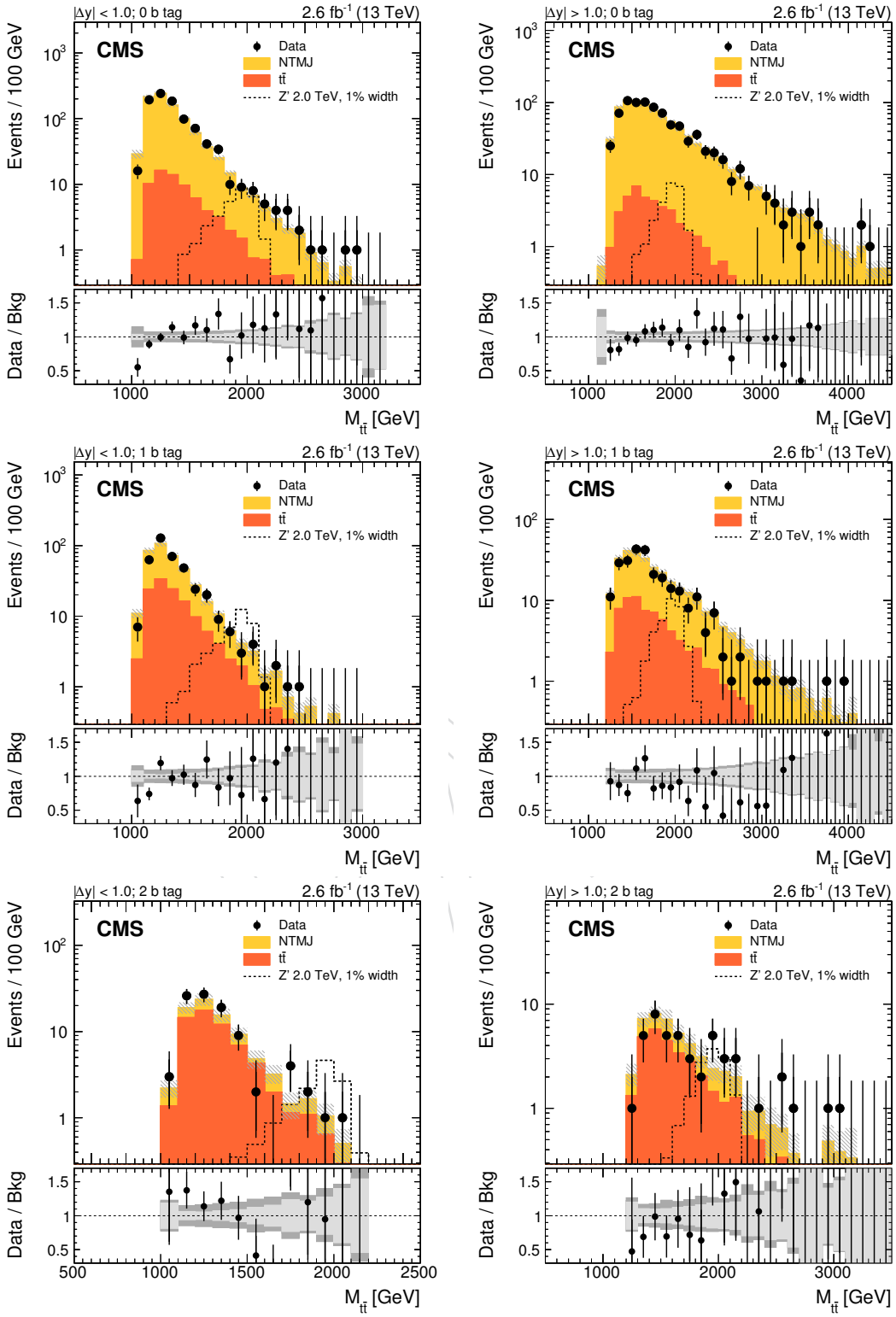

Figure 5: Distributions in $M_{t\bar{t}}$ for data and expected background, for events passing the signal selection of the fully hadronic analysis after the maximum likelihood fit. Distributions are shown for the regions with $|\Delta y| < 1.0$ (left) and $|\Delta y| > 1.0$ (right), for 0, 1, or 2 subjet b tags (from uppermost to lowest). The signal templates are normalized to a cross section of 1 pb. The uncertainties associated with the background expectation include the statistical and all post-fit systematic uncertainties. The lower panel in each figure shows the ratio of data to predicted SM background, with the statistical (light gray) and total (dark gray) uncertainties shown separately.

Table 3: Numbers of events in the signal region for the lepton+jets analysis. The expected yields for SM backgrounds are obtained from the maximum likelihood fit to the data described in Section 6.4. The uncertainties reported in the total expected background include the statistical uncertainties in the simulation and all the posterior systematic uncertainties. For the W+jets background, LF (HF) indicates contributions from W bosons produced in association with light-flavor (heavy-flavor) jets.

	μ+jets signal region		
Process	1 t tag	0 t tags, 1 b tag	0 t tags, 0 b tags
$t\bar{t}$	218 ± 28	7602 ± 826	1965 ± 229
W+jets (LF)	27 ± 4	547 ± 54	4675 ± 377
W+jets (HF)	4 ± 1	333 ± 30	780 ± 65
Other	9 ± 2	682 ± 111	635 ± 85
Total background	258 ± 29	9164 ± 856	8055 ± 541
Data	252	9230	7966

	e+jets signal region		
Process	1 t tag	0 t tags, 1 b tag	0 t tags, 0 b tags
$t\bar{t}$	119 ± 15	1016 ± 124	248 ± 32
W+jets (LF)	13 ± 2	97 ± 10	684 ± 58
W+jets (HF)	2 ± 1	44 ± 4	84 ± 8
Other	4 ± 1	103 ± 18	74 ± 10
Total background	138 ± 16	1260 ± 129	1090 ± 78
Data	142	1217	1005

Table 4: Number of events in the signal region for the fully hadronic analysis. The expected yields for SM backgrounds are obtained from the maximum likelihood fit to data described in the text. The uncertainties reported for the total expected background include the statistical uncertainties on the simulation and all the posterior systematic uncertainties.

	$\lvert\Delta y\rvert > 1.0$ signal region		
Process	0 b tags	1 b tag	2 b tags
SM $t\bar{t}$	34 ± 4.3	62 ± 5.8	28 ± 3.8
NTMJ	787 ± 6.2	215 ± 4.7	15 ± 1.9
Total background	821 ± 7.5	278 ± 7.4	43 ± 4.2
Data	830	264	46

	$\lvert\Delta y\rvert < 1.0$ signal region		
Process	0 b tags	1 b tag	2 b tags
SM $t\bar{t}$	66 ± 7.1	121 ± 10	60 ± 7.0
NTMJ	817 ± 8.0	248 ± 7.0	19 ± 1.7
Total background	882 ± 11	369 ± 12	79 ± 7.3
Data	925	387	94

7 Results

The number of events observed in data and expected from SM processes after the background fit are given in Tables 3 and 4 for the six categories in the signal region of the lepton+jets and fully hadronic channels, respectively. The invariant mass distribution of the reconstructed $t\bar{t}$

pair is shown in Fig. 4 (Fig. 5) for data and the expected SM backgrounds in the lepton+jets (fully hadronic) signal-region categories after the background fit. Good agreement between data and background prediction is observed within the estimated systematic uncertainties. The modeling of the data in background-enriched samples is verified using kinematic distributions for leptons, jets, and the reconstructed leptonically and hadronically decaying top quarks in each of the individual categories considered in the analysis. The small differences are covered by the systematic uncertainties. For the lepton+jets channel, some discrepancies are observed at large $M_{t\bar{t}}$ in the distributions in categories where the W+jets background dominates. These discrepancies are related to missing higher-order corrections in the simulated events, and have little impact on the results, as these categories are less sensitive than those dominated by $t\bar{t}$. Dedicated cross checks have confirmed that the localized discrepancies visible in Figs. 4 and 5 may be attributed to statistical fluctuations. The sensitivity of this analysis is driven by the 1 t tag categories in the lepton+jets channel, and the 2 b tag categories in the fully hadronic channel, which have the highest signal-to-background ratios.

We proceed to set exclusion limits on different benchmark models for $t\bar{t}$ resonances. Four extensions to the SM are considered in the statistical analysis: a Z' boson decaying exclusively to $t\bar{t}$ with a relative decay width (Γ/M) of 1%, 10%, or 30%, and a KK gluon resonance in the RS model. The cross sections for Z' production are taken from NLO order calculations [76]. The leading order (LO) predictions for the KK gluon cross sections are multiplied by a factor of 1.3 to account for higher-order corrections [77].

Limits are extracted on the cross sections for the various signal hypotheses using the distributions in Figs. 4 and 5. By varying the nuisance parameters within their prior distribution functions, pseudo-experiments are performed to estimate the 68% and 95% CL (1 and 2 standard deviations) expected limits in the median results. The combined results, including observed limits on the resonant production cross sections, are shown in Fig. 6, and tabulated in Tables 5–9. The combination of the lepton+jets and fully hadronic channels significantly improves the exclusion limits relative to previous results for all models, except for those using a width of 1%. Starting from the lower mass exclusion limit of 0.5 TeV, masses are excluded up to 4 TeV for the 30% width Z' samples, up to 3.9 TeV for the 10% width Z', and up to 3.3 TeV for the RS KK gluon hypotheses, at the 95% CL. These limits are close to the point where the parton luminosity at low $t\bar{t}$ mass dominates the mass distribution by enhancing the off-shell contribution and reducing the resonant contribution, modifying the behavior of the signal model from resonant-like to nonresonant-like. Because of this, a different analysis strategy should be considered in future searches, in order to be sensitive to such non-resonant production at large $M_{t\bar{t}}$. Table 5 shows the exclusion limits obtained for the two channels and for their combination. Figure 7 presents the Z' limits as a function of width instead of mass.

Table 5: Comparison of mass exclusion results (in TeV) for the individual channels and for their combination.

	Excluded mass ranges [TeV]							
	Z' ($\Gamma/M = 1\%$)		Z' ($\Gamma/M = 10\%$)		Z' ($\Gamma/M = 30\%$)		RS KK Gluon	
Result	Exp.	Obs.	Exp.	Obs.	Exp.	Obs.	Exp.	Obs.
Lepton+jets	0.6 – 2.1	0.6 – 2.3	0.5 – 3.5	0.5 – 3.4	0.5 – 4.0	0.5 – 4.0	0.5 – 2.9	0.5 – 2.9
Fully hadronic	1.2 – 1.8	1.4 – 1.8	1.0 – 3.2	1.0 – 3.5	1.0 – 3.7	1.0 – 4.0	1.0 – 2.6	1.0 – 2.4
Combined	0.6 – 2.4	0.6 – 2.5	0.5 – 3.7	0.5 – 3.9	0.5 – 4.0	0.5 – 4.0	0.5 – 3.1	0.5 – 3.3

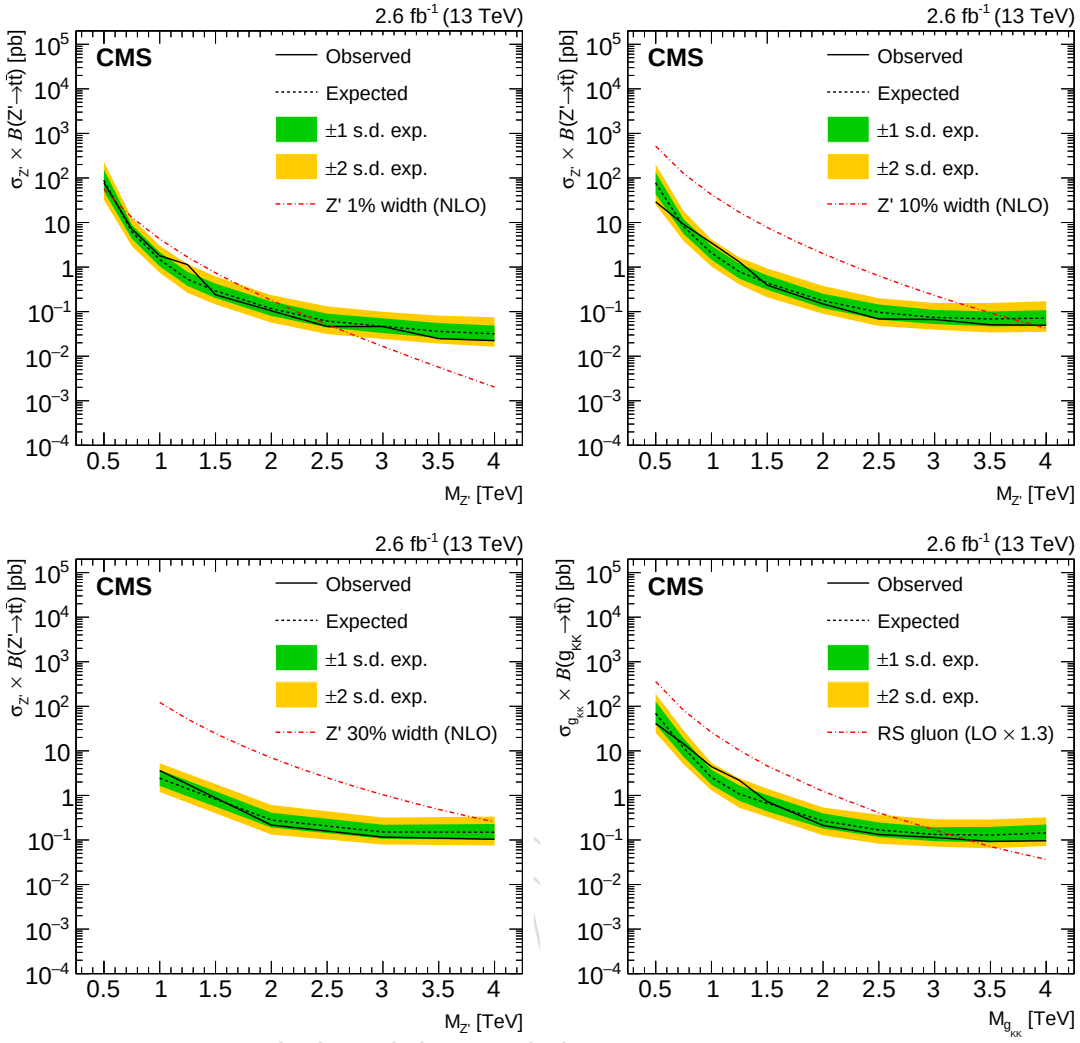

Figure 6: Observed and expected upper limits at 95% CL on the product of the production cross section and branching fractions for the full combination of the analysis results, shown as function of the resonance mass. Limits are set using four extensions to the SM : (upper left) a Z' boson with Γ/M of 1%, (upper right) a Z' boson with Γ/M of 10%, (lower left) a Z' boson with Γ/M of 30% and (lower right) a KK excitation of a gluon in the RS model. The corresponding theoretical prediction as a function of the resonance mass is shown as a dot-dashed curve.

8 Summary

A model-independent search for the production of heavy spin-1 or spin-2 resonances decaying into $\mathrm{t\bar{t}}$ final states has been conducted. The data correspond to an integrated luminosity of 2.6 fb^{-1} collected with the CMS detector in proton-proton collisions at $\sqrt{s} = 13$ TeV at the LHC. The analysis is designed to have high sensitivity at resonance masses above 1 TeV, where final-state decay products become collimated because of the large Lorentz boosts of the top quarks. The analysis method provides an in-situ measurement of the data-to-simulation scale factor for the t tagging efficiency and the normalization of the main backgrounds. No evidence for massive resonances that decay to $\mathrm{t\bar{t}}$ is found. Limits at 95% CL are set on the production cross section of new spin-1 particles decaying to $\mathrm{t\bar{t}}$ with relative decay widths that are either narrow or wide compared with the detector resolution.

In addition, limits are set on the production of particles in benchmark models beyond the stan-

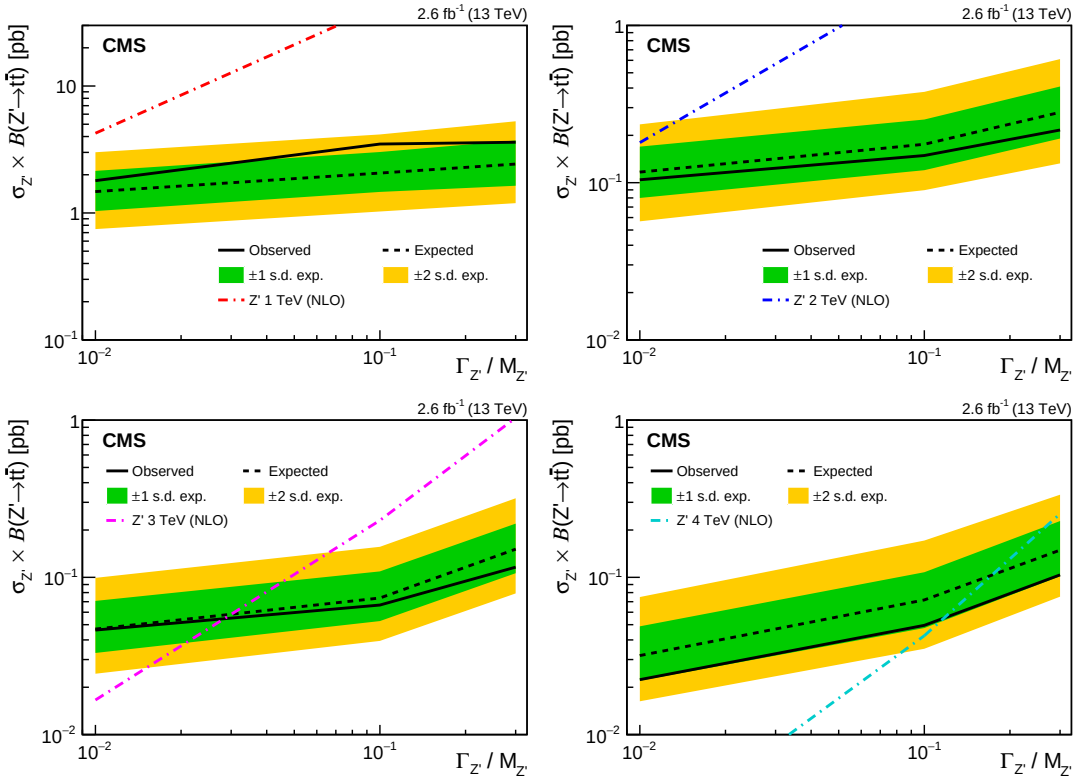

Figure 7: Expected and observed limits presented as a function of width, for $M_{Z'} = 1$, 2, 3, 4 TeV. The corresponding theoretical prediction as a function of width is shown as a dot-dashed curve in each case.

dard model. Topcolor Z′ bosons with relative widths Γ/M of 1%, 10%, and 30% are excluded for mass ranges of 0.6–2.5, 0.5–3.9, and 0.5–4.0 TeV, respectively. Kaluza–Klein excitations of a gluon with masses in the range 0.5–3.3 TeV in the Randall–Sundrum model are also excluded. This search presents limits on Z′ bosons as a function of the relative width of the resonance in the range from 1–30%, for the first time in CMS.

This analysis yields approximately the same sensitivity as the previous search based on 8 TeV data [27] (corresponding to an integrated luminosity of 19.7 fb^{-1}) for resonance masses in the range 1.0–2.0 TeV. At higher resonance masses, the present analysis is significantly more sensitive. Previous lower mass limits on the Z′ with 10% relative width and the Kaluza–Klein gluon were 2.9 and 2.8 TeV, respectively. The present analysis extends the lower mass limits to 3.9 and 3.3 TeV, respectively, for these models.

Table 6: Expected and observed cross section limits at 95% CL, for the 1% width Z′ resonance hypothesis.

Mass [TeV]	Observed limits [pb]	Expected limits [pb]				
		-2σ	-1σ	Median	$+1\sigma$	$+2\sigma$
0.5	78	32	50	88	150	230
0.75	7.1	2.9	4.3	6.1	8.8	13
1.0	1.8	0.75	1.0	1.5	2.2	3.0
1.25	1.1	0.26	0.38	0.53	0.78	1.2
1.5	0.24	0.15	0.20	0.29	0.43	0.62
2.0	0.10	0.057	0.080	0.12	0.17	0.24
2.5	0.046	0.031	0.044	0.061	0.090	0.13
3.0	0.046	0.024	0.033	0.047	0.071	0.099
3.5	0.025	0.019	0.026	0.036	0.055	0.081
4.0	0.022	0.016	0.022	0.032	0.049	0.075

Table 7: Expected and observed cross section limits at 95% CL, for the 10% width Z′ resonance hypothesis.

Mass [TeV]	Observed limits [pb]	Expected limits [pb]				
		-2σ	-1σ	Median	$+1\sigma$	$+2\sigma$
0.5	29	25	43	77	130	200
0.75	9.1	3.9	5.6	8.1	12	18
1.0	3.5	1.0	1.5	2.1	3.0	4.2
1.25	1.3	0.41	0.55	0.79	1.2	1.6
1.5	0.39	0.21	0.31	0.44	0.65	0.93
2.0	0.15	0.089	0.12	0.18	0.25	0.38
2.5	0.068	0.048	0.066	0.097	0.15	0.20
3.0	0.067	0.039	0.053	0.074	0.11	0.16
3.5	0.051	0.034	0.047	0.069	0.10	0.16
4.0	0.050	0.035	0.048	0.072	0.11	0.17

Table 8: Expected and observed cross section limits at 95% CL, for the 30% width Z′ resonance hypothesis.

Mass [TeV]	Observed limits [pb]	Expected limits [pb]				
		-2σ	-1σ	Median	$+1\sigma$	$+2\sigma$
1.0	3.6	1.2	1.6	2.4	3.7	5.3
2.0	0.22	0.13	0.19	0.28	0.41	0.61
3.0	0.12	0.080	0.11	0.15	0.22	0.32
4.0	0.10	0.075	0.10	0.15	0.23	0.34

Table 9: Expected and observed cross section limits at 95% CL, for the RS KK gluon hypothesis.

Mass [TeV]	Observed limits [pb]	Expected limits [pb]				
		-2σ	-1σ	Median	$+1\sigma$	$+2\sigma$
0.5	41	26	40	69	130	190
0.75	14	5.0	7.3	12	19	29
1.0	4.4	1.3	1.7	2.5	3.8	5.3
1.25	2.2	0.53	0.76	1.1	1.7	2.4
1.5	0.73	0.33	0.44	0.67	1.0	1.4
2.0	0.21	0.13	0.18	0.27	0.40	0.54
2.5	0.13	0.082	0.12	0.17	0.25	0.37
3.0	0.11	0.071	0.094	0.13	0.19	0.29
3.5	0.093	0.065	0.088	0.13	0.20	0.29
4.0	0.096	0.073	0.099	0.14	0.22	0.32

Acknowledgments

We congratulate our colleagues in the CERN accelerator departments for the excellent performance of the LHC and thank the technical and administrative staffs at CERN and at other CMS institutes for their contributions to the success of the CMS effort. In addition, we gratefully acknowledge the computing centers and personnel of the Worldwide LHC Computing Grid for delivering so effectively the computing infrastructure essential to our analyses. Finally, we acknowledge the enduring support for the construction and operation of the LHC and the CMS detector provided by the following funding agencies: the Austrian Federal Ministry of Science, Research and Economy and the Austrian Science Fund; the Belgian Fonds de la Recherche Scientifique, and Fonds voor Wetenschappelijk Onderzoek; the Brazilian Funding Agencies (CNPq, CAPES, FAPERJ, and FAPESP); the Bulgarian Ministry of Education and Science; CERN; the Chinese Academy of Sciences, Ministry of Science and Technology, and National Natural Science Foundation of China; the Colombian Funding Agency (COLCIENCIAS); the Croatian Ministry of Science, Education and Sport, and the Croatian Science Foundation; the Research Promotion Foundation, Cyprus; the Secretariat for Higher Education, Science, Technology and Innovation, Ecuador; the Ministry of Education and Research, Estonian Research Council via IUT23-4 and IUT23-6 and European Regional Development Fund, Estonia; the Academy of Finland, Finnish Ministry of Education and Culture, and Helsinki Institute of Physics; the Institut National de Physique Nucléaire et de Physique des Particules / CNRS, and Commissariat à l'Énergie Atomique et aux Énergies Alternatives / CEA, France; the Bundesministerium für Bildung und Forschung, Deutsche Forschungsgemeinschaft, and Helmholtz-Gemeinschaft Deutscher Forschungszentren, Germany; the General Secretariat for Research and Technology, Greece; the National Scientific Research Foundation, and National Innovation Office, Hungary; the Department of Atomic Energy and the Department of Science and Technology, India; the Institute for Studies in Theoretical Physics and Mathematics, Iran; the Science Foundation, Ireland; the Istituto Nazionale di Fisica Nucleare, Italy; the Ministry of Science, ICT and Future Planning, and National Research Foundation (NRF), Republic of Korea; the Lithuanian Academy of Sciences; the Ministry of Education, and University of Malaya (Malaysia); the Mexican Funding Agencies (BUAP, CINVESTAV, CONACYT, LNS, SEP, and UASLP-FAI); the Ministry of Business, Innovation and Employment, New Zealand; the Pakistan Atomic Energy Commission; the Ministry of Science and Higher Education and the National Science Centre, Poland; the Fundação para a Ciência e a Tecnologia, Portugal; JINR, Dubna; the Ministry of Education and Science of the Russian Federation, the Federal Agency of Atomic Energy of the Russian Federation, Russian Academy of Sciences, and the Russian Foundation for Basic Research; the Ministry of Education, Science and Technological Development of Serbia; the Secretaría de Estado de Investigación, Desarrollo e Innovación and Programa Consolider-Ingenio 2010, Spain; the Swiss Funding Agencies (ETH Board, ETH Zurich, PSI, SNF, UniZH, Canton Zurich, and SER); the Ministry of Science and Technology, Taipei; the Thailand Center of Excellence in Physics, the Institute for the Promotion of Teaching Science and Technology of Thailand, Special Task Force for Activating Research and the National Science and Technology Development Agency of Thailand; the Scientific and Technical Research Council of Turkey, and Turkish Atomic Energy Authority; the National Academy of Sciences of Ukraine, and State Fund for Fundamental Researches, Ukraine; the Science and Technology Facilities Council, UK; the US Department of Energy, and the US National Science Foundation.

Individuals have received support from the Marie-Curie programme and the European Research Council and EPLANET (European Union); the Leventis Foundation; the A. P. Sloan Foundation; the Alexander von Humboldt Foundation; the Belgian Federal Science Policy Office; the Fonds pour la Formation à la Recherche dans l'Industrie et dans l'Agriculture (FRIA-

Belgium); the Agentschap voor Innovatie door Wetenschap en Technologie (IWT-Belgium); the Ministry of Education, Youth and Sports (MEYS) of the Czech Republic; the Council of Science and Industrial Research, India; the HOMING PLUS programme of the Foundation for Polish Science, cofinanced from European Union, Regional Development Fund, the Mobility Plus programme of the Ministry of Science and Higher Education, the National Science Center (Poland), contracts Harmonia 2014/14/M/ST2/00428, Opus 2013/11/B/ST2/04202, 2014/13/B/ST2/02543 and 2014/15/B/ST2/03998, Sonata-bis 2012/07/E/ST2/01406; the Thalis and Aristeia programmes cofinanced by EU-ESF and the Greek NSRF; the National Priorities Research Program by Qatar National Research Fund; the Programa Clarín-COFUND del Principado de Asturias; the Rachadapisek Sompot Fund for Postdoctoral Fellowship, Chulalongkorn University and the Chulalongkorn Academic into Its 2nd Century Project Advancement Project (Thailand); and the Welch Foundation, contract C-1845.

References

[1] J. L. Rosner, "Prominent decay modes of a leptophobic Z'", *Phys. Lett. B* **387** (1996) 113, doi:10.1016/0370-2693(96)01022-2, arXiv:hep-ph/9607207.

[2] K. R. Lynch, S. Mrenna, M. Narain, and E. H. Simmons, "Finding Z' bosons coupled preferentially to the third family at CERN LEP and the Fermilab Tevatron", *Phys. Rev. D* **63** (2001) 035006, doi:10.1103/PhysRevD.63.035006, arXiv:hep-ph/0007286.

[3] M. Carena, A. Daleo, B. A. Dobrescu, and T. M. P. Tait, "Z' gauge bosons at the Fermilab Tevatron", *Phys. Rev. D* **70** (2004) 093009, doi:10.1103/PhysRevD.70.093009, arXiv:hep-ph/0408098.

[4] C. T. Hill, "Topcolor top quark condensation in a gauge extension of the standard model", *Phys. Lett. B* **266** (1991) 419, doi:10.1016/0370-2693(91)91061-Y.

[5] R. M. Harris and S. Jain, "Cross sections for leptophobic topcolor Z' decaying to top-antitop", *Eur. Phys. J. C* **72** (2012) 2072, doi:10.1140/epjc/s10052-012-2072-4, arXiv:1112.4928.

[6] C. T. Hill and S. J. Parke, "Top production: Sensitivity to new physics", *Phys. Rev. D* **49** (1994) 4454, doi:10.1103/PhysRevD.49.4454, arXiv:hep-ph/9312324.

[7] C. T. Hill, "Topcolor assisted technicolor", *Phys. Lett. B* **345** (1995) 483, doi:10.1016/0370-2693(94)01660-5, arXiv:hep-ph/9411426.

[8] P. H. Frampton and S. L. Glashow, "Chiral color: An alternative to the standard model", *Phys. Lett. B* **190** (1987) 157, doi:10.1016/0370-2693(87)90859-8.

[9] D. Choudhury, R. M. Godbole, R. K. Singh, and K. Wagh, "Top production at the Tevatron/LHC and nonstandard, strongly interacting spin one particles", *Phys. Lett. B* **657** (2007) 69, doi:10.1016/j.physletb.2007.09.057, arXiv:0705.1499.

[10] R. M. Godbole and D. Choudhury, "Nonstandard, strongly interacting spin one $t\bar{t}$ resonances", in *Proceedings, 34th International Conference on High Energy Physics (ICHEP 2008): Philadelphia, Pennsylvania, July 30-August 5, 2008*. 2008. arXiv:0810.3635.

[11] D. Dicus, A. Stange, and S. Willenbrock, "Higgs decay to top quarks at hadron colliders", *Phys. Lett. B* **333** (1994) 126, doi:10.1016/0370-2693(94)91017-0, arXiv:hep-ph/9404359.

[12] K. Agashe et al., "CERN LHC signals from warped extra dimensions", *Phys. Rev. D* **77** (2008) 015003, doi:10.1103/PhysRevD.77.015003, arXiv:hep-ph/0612015.

[13] K. Agashe et al., "CERN LHC signals for warped electroweak neutral gauge bosons", *Phys. Rev. D* **76** (2007) 115015, doi:10.1103/PhysRevD.76.115015, arXiv:0709.0007.

[14] H. Davoudiasl, J. L. Hewett, and T. G. Rizzo, "Phenomenology of the Randall-Sundrum Gauge Hierarchy Model", *Phys. Rev. Lett.* **84** (2000) 2080, doi:10.1103/PhysRevLett.84.2080, arXiv:hep-ph/9909255.

[15] L. Randall and R. Sundrum, "Large Mass Hierarchy from a Small Extra Dimension", *Phys. Rev. Lett.* **83** (1999) 3370, doi:10.1103/PhysRevLett.83.3370, arXiv:hep-ph/9905221.

[16] L. Randall and R. Sundrum, "An Alternative to Compactification", *Phys. Rev. Lett.* **83** (1999) 4690, doi:10.1103/PhysRevLett.83.4690, arXiv:hep-th/9906064.

[17] CDF Collaboration, "A search for resonant production of $t\bar{t}$ pairs in 4.8 fb^{-1} of integrated luminosity of $p\bar{p}$ collisions at $\sqrt{s} = 1.96$ TeV", *Phys. Rev. D* **84** (2011) 072004, doi:10.1103/PhysRevD.84.072004, arXiv:1107.5063.

[18] D0 Collaboration, "Search for a narrow $t\bar{t}$ resonance in $p\bar{p}$ collisions at $\sqrt{s} = 1.96$ TeV", *Phys. Rev. D* **85** (2012) 051101, doi:10.1103/PhysRevD.85.051101, arXiv:1111.1271.

[19] CMS Collaboration, "Search for anomalous $\mathrm{t\bar{t}}$ production in the highly-boosted all-hadronic final state", *JHEP* **09** (2012) 029, doi:10.1007/JHEP09(2012)029, arXiv:1204.2488.

[20] ATLAS Collaboration, "Search for resonances decaying into top-quark pairs using fully hadronic decays in pp collisions with ATLAS at $\sqrt{s} = 7$ TeV", *JHEP* **01** (2013) 116, doi:10.1007/JHEP01(2013)116, arXiv:1211.2202.

[21] ATLAS Collaboration, "A search for $t\bar{t}$ resonances in the lepton plus jets final state with ATLAS using 4.7 fb^{-1} of pp collisions at $\sqrt{s} = 7$ TeV", *Phys. Rev. D* **88** (2013) 012004, doi:10.1103/PhysRevD.88.012004, arXiv:1305.2756.

[22] ATLAS Collaboration, "A search for $t\bar{t}$ resonances in lepton+jets events with highly boosted top quarks collected in pp collisions at $\sqrt{s} = 7$ TeV with the ATLAS detector", *JHEP* **09** (2012) 041, doi:10.1007/JHEP09(2012)041, arXiv:1207.2409.

[23] CMS Collaboration, "Search for resonant $\mathrm{t\bar{t}}$ production in lepton+jets events in pp collisions at $\sqrt{s} = 7$ TeV", *JHEP* **12** (2012) 015, doi:10.1007/JHEP12(2012)015, arXiv:1209.4397.

[24] CMS Collaboration, "Search for Z' resonances decaying to $t\bar{t}$ in dilepton+jets final states in pp collisions at $\sqrt{s} = 7$ TeV", *Phys. Rev. D* **87** (2013) 072002, doi:10.1103/PhysRevD.87.072002, arXiv:1211.3338.

[25] CMS Collaboration, "Searches for new physics using the $t\bar{t}$ invariant mass distribution in pp collisions at $\sqrt{s} = 8$ TeV", *Phys. Rev. Lett.* **111** (2013) 211804, doi:10.1103/PhysRevLett.111.211804, arXiv:1309.2030.

[26] ATLAS Collaboration, "A search for $\mathrm{t\bar{t}}$ resonances using lepton-plus-jets events in proton-proton collisions at $\sqrt{s} = 8$ TeV with the ATLAS detector", *JHEP* **08** (2015) 148, doi:10.1007/JHEP08(2015)148, arXiv:1505.07018.

[27] CMS Collaboration, "Search for resonant $\mathrm{t\bar{t}}$ production in proton-proton collisions at $\sqrt{s} = 8$ TeV", *Phys. Rev. D* **93** (2016) 012001, doi:10.1103/PhysRevD.93.012001, arXiv:1506.03062.

[28] G. Altarelli, B. Mele, and M. Ruiz-Altaba, "Searching for new heavy vector bosons in $p\bar{p}$ colliders", *Z. Phys. C* **45** (1989) 109, doi:10.1007/BF01556677. [Erratum: doi:10.1007/BF01552335].

[29] CMS Collaboration, "The CMS experiment at the CERN LHC", *JINST* **3** (2008) S08004, doi:10.1088/1748-0221/3/08/S08004.

[30] CMS Collaboration, "Particle–Flow Event Reconstruction in CMS and Performance for Jets, Taus, and $E_{\mathrm{T}}^{\mathrm{miss}}$", CMS Physics Analysis Summary CMS-PAS-PFT-09-001, 2009.

[31] CMS Collaboration, "Commissioning of the Particle-flow Event Reconstruction with the first LHC collisions recorded in the CMS detector", CMS Physics Analysis Summary CMS-PAS-PFT-10-001, 2010.

[32] CMS Collaboration, "Description and performance of track and primary-vertex reconstruction with the CMS tracker", *JINST* **9** (2014) P10009, doi:10.1088/1748-0221/9/10/P10009, arXiv:1405.6569.

[33] CMS Collaboration, "Performance of CMS muon reconstruction in pp collision events at $\sqrt{s} = 7$ TeV", *JINST* **7** (2012) P10002, doi:10.1088/1748-0221/7/10/P10002, arXiv:1206.4071.

[34] CMS Collaboration, "Performance of electron reconstruction and selection with the CMS Detector in proton-proton collisions at $\sqrt{s} = 8$ TeV", *JINST* **10** (2015) P06005, doi:10.1088/1748-0221/10/06/P06005, arXiv:1502.02701.

[35] M. Cacciari, G. P. Salam, and G. Soyez, "The anti-k_t jet clustering algorithm", *JHEP* **04** (2008) 063, doi:10.1088/1126-6708/2008/04/063, arXiv:0802.1189.

[36] M. Cacciari, G. P. Salam, and G. Soyez, "FastJet user manual", *Eur. Phys. J. C* **72** (2012) 1896, doi:10.1140/epjc/s10052-012-1896-2, arXiv:1111.6097.

[37] M. Cacciari, G. P. Salam, and G. Soyez, "The catchment area of jets", *JHEP* **04** (2008) 005, doi:10.1088/1126-6708/2008/04/005, arXiv:0802.1188.

[38] CMS Collaboration, "Determination of jet energy calibration and transverse momentum resolution in CMS", *JINST* **6** (2011) P11002, doi:10.1088/1748-0221/6/11/P11002, arXiv:1107.4277.

[39] CMS Collaboration, "Identification of b-quark jets with the CMS experiment", *JINST* **8** (2013) P04013, doi:10.1088/1748-0221/8/04/P04013, arXiv:1211.4462.

[40] CMS Collaboration, "Identification of b quark jets at the CMS experiment in the LHC Run 2", CMS Physics Analysis Summary CMS-PAS-BTV-15-001, 2016.

[41] CMS Collaboration, "Top Tagging with New Approaches", CMS Physics Analysis Summary CMS-PAS-JME-15-002, 2016.

[42] Y. L. Dokshitzer, G. D. Leder, S. Moretti, and B. R. Webber, "Better jet clustering algorithms", *JHEP* **08** (1997) 001, doi:10.1088/1126-6708/1997/08/001, arXiv:hep-ph/9707323.

[43] M. Wobisch and T. Wengler, "Hadronization corrections to jet cross sections in deep-inelastic scattering", (1998). arXiv:hep-ph/9907280.

[44] M. Dasgupta, A. Fregoso, S. Marzani, and G. P. Salam, "Towards an understanding of jet substructure", *JHEP* **09** (2013) 029, doi:10.1007/JHEP09(2013)029, arXiv:1307.0007.

[45] CMS Collaboration, "Study of Pileup Removal Algorithms for Jets", CMS Physics Analysis Summary CMS-PAS-JME-14-001, 2014.

[46] A. J. Larkoski, S. Marzani, G. Soyez, and J. Thaler, "Soft drop", *JHEP* **05** (2014) 146, doi:10.1007/JHEP05(2014)146, arXiv:1402.2657.

[47] J. Thaler and K. Van Tilburg, "Identifying boosted objects with N-subjettiness", *JHEP* **03** (2011) 015, doi:10.1007/JHEP03(2011)015, arXiv:1011.2268.

[48] J. Thaler and K. Van Tilburg, "Maximizing boosted top identification by minimizing *N*-subjettiness", *JHEP* **02** (2012) 093, doi:10.1007/JHEP02(2012)093, arXiv:1108.2701.

[49] J. Alwall et al., "The automated computation of tree-level and next-to-leading order differential cross sections, and their matching to parton shower simulations", *JHEP* **07** (2014) 079, doi:10.1007/JHEP07(2014)079, arXiv:1405.0301.

[50] T. Sjöstrand, S. Mrenna, and P. Z. Skands, "PYTHIA 6.4 physics and manual", *JHEP* **05** (2006) 026, doi:10.1088/1126-6708/2006/05/026, arXiv:hep-ph/0603175.

[51] T. Sjöstrand et al., "An introduction to PYTHIA 8.2", *Comput. Phys. Commun.* **191** (2015) 159, doi:10.1016/j.cpc.2015.01.024, arXiv:1410.3012.

[52] M. L. Mangano, M. Moretti, F. Piccinini, and M. Treccani, "Matching matrix elements and shower evolution for top-quark production in hadronic collisions", *JHEP* **01** (2007) 013, doi:10.1088/1126-6708/2007/01/013, arXiv:hep-ph/0611129.

[53] P. Nason, "A new method for combining NLO QCD with shower Monte Carlo algorithms", *JHEP* **11** (2004) 040, doi:10.1088/1126-6708/2004/11/040, arXiv:hep-ph/0409146.

[54] S. Frixione, P. Nason, and C. Oleari, "Matching NLO QCD computations with Parton Shower simulations: the POWHEG method", *JHEP* **11** (2007) 070, doi:10.1088/1126-6708/2007/11/070, arXiv:0709.2092.

[55] S. Alioli, P. Nason, C. Oleari, and E. Re, "A general framework for implementing NLO calculations in shower Monte Carlo programs: the POWHEG BOX", *JHEP* **06** (2010) 043, doi:10.1007/JHEP06(2010)043, arXiv:1002.2581.

[56] S. Frixione, P. Nason, and G. Ridolfi, "A positive-weight next-to-leading-order Monte Carlo for heavy flavour hadroproduction", *JHEP* **09** (2007) 126, doi:10.1088/1126-6708/2007/09/126, arXiv:0707.3088.

[57] E. Re, "Single-top Wt-channel production matched with parton showers using the POWHEG method", *Eur. Phys. J. C* **71** (2011) 1547, doi:10.1140/epjc/s10052-011-1547-z, arXiv:1009.2450.

[58] M. Czakon and A. Mitov, "Top++: A program for the calculation of the top-pair cross-section at hadron colliders", *Comput. Phys. Commun.* **185** (2014) 2930, doi:10.1016/j.cpc.2014.06.021, arXiv:1112.5675.

[59] Y. Li and F. Petriello, "Combining QCD and electroweak corrections to dilepton production in FEWZ", *Phys. Rev. D* **86** (2012) 094034, doi:10.1103/PhysRevD.86.094034, arXiv:1208.5967.

[60] P. Kant et al., "HatHor for single top-quark production: Updated predictions and uncertainty estimates for single top-quark production in hadronic collisions", *Comput. Phys. Commun.* **191** (2015) 74, doi:10.1016/j.cpc.2015.02.001, arXiv:1406.4403.

[61] N. Kidonakis, "NNLL threshold resummation for top-pair and single-top production", *Phys. Part. Nucl.* **45** (2014) 714, doi:10.1134/S1063779614040091, arXiv:1210.7813.

[62] J. M. Campbell and R. K. Ellis, "MCFM for the Tevatron and the LHC", *Nucl. Phys. Proc. Suppl.* **205** (2010) 10, doi:10.1016/j.nuclphysbps.2010.08.011, arXiv:1007.3492.

[63] NNPDF Collaboration, "Parton distributions for the LHC Run II", *JHEP* **04** (2015) 040, doi:10.1007/JHEP04(2015)040, arXiv:1410.8849.

[64] CMS Collaboration, "Event generator tunes obtained from underlying event and multiparton scattering measurements", *Eur. Phys. J. C* **76** (2016) 155, doi:10.1140/epjc/s10052-016-3988-x, arXiv:1512.00815.

[65] P. Skands, S. Carrazza, and J. Rojo, "Tuning PYTHIA 8.1: the Monash 2013 Tune", *Eur. Phys. J. C* **74** (2014) 3024, doi:10.1140/epjc/s10052-014-3024-y, arXiv:1404.5630.

[66] T. Müller, J. Ott, and J. Wagner-Kuhr, "theta - a framework for template-based modeling and inference", 2010.

[67] J. M. Campbell, R. K. Ellis, and C. Williams, "Vector boson pair production at the LHC", *JHEP* **07** (2011) 018, doi:10.1007/JHEP07(2011)018, arXiv:1105.0020.

[68] T. Gehrmann et al., "W^+W^- Production at Hadron Colliders in Next-to-Next-to-Leading-Order QCD", *Phys. Rev. Lett.* **113** (2014) 212001, doi:10.1103/PhysRevLett.113.212001, arXiv:1408.5243.

[69] N. Kidonakis, "Top Quark Production", *Proceedings, Helmholtz International Summer School on Physics of Heavy Quarks and Hadrons (HQ 2013)* (2014) 139, doi:10.3204/DESY-PROC-2013-03/Kidonakis, arXiv:1311.0283.

[70] M. Aliev et al., "HATHOR: HAdronic Top and Heavy quarks crOss section calculatoR", *Comput. Phys. Commun.* **182** (2011) 1034, doi:10.1016/j.cpc.2010.12.040, arXiv:1007.1327.

[71] M. Botje et al., "The PDF4LHC Working Group Interim Recommendations", (2011). arXiv:1101.0538.

[72] CMS Collaboration, "CMS Luminosity Measurement for the 2015 Data Taking Period", CMS Physics Analysis Summary CMS-PAS-LUM-15-001, 2016.

[73] CMS Collaboration, "Measurement of the inelastic proton-proton cross section at $\sqrt{s} = 13$ TeV", CMS Physics Analysis Summary CMS-PAS-FSQ-15-005, 2016.

[74] A. O'Hagan and J. J. Forster, "Kendall's Advanced Theory of Statistics. Vol. 2B: Bayesian Inference". Arnold, London, 2004. doi:10.1111/j.1467-985X.2004.00347_15.x.

[75] R. J. Barlow and C. Beeston, "Fitting using finite Monte Carlo samples", *Comput. Phys. Commun.* **77** (1993) 219, doi:10.1016/0010-4655(93)90005-W.

[76] R. Bonciani et al., "Electroweak top-quark pair production at the LHC with Z' bosons to NLO QCD in POWHEG", *JHEP* **02** (2016) 141, doi:10.1007/JHEP02(2016)141, arXiv:1511.08185.

[77] J. Gao et al., "Next-to-leading order QCD corrections to the heavy resonance production and decay into top quark pair at the LHC", *Phys. Rev. D* **82** (2010) 014020, doi:10.1103/PhysRevD.82.014020, arXiv:1004.0876.